Supporting Material for

Axonal Transport: How High Microtubule Density Can Compensate for Boundary Effects in Small-Caliber Axons

Juliana C. Wortman,[†] Uttam M. Shrestha,[†] Devin M. Barry,[‡] Michael L. Garcia,[§] Steven P. Gross,[†¶] and Clare C. Yu[†]*

[†]Department of Physics and Astronomy, University of California, Irvine, Irvine, CA 92697; [‡]Center for the Study of Itch, Washington University School of Medicine, St. Louis, MO 63110; [§]Biological Sciences, University of Missouri, Columbia, MO 65211; [¶]Department of Developmental and Cell Biology, University of California, Irvine, Irvine, CA 92697.

In this supplement, we describe the basic algorithm that we have used to simulate the cargo dynamics in multiple microtubules as well as the implementation of cargo-protein interactions. We also describe how we analyzed electron micrographs to obtain the distribution of microtubules. In Section 1, we describe the formalism of the wall effect. In Section 2, we introduce the transport of a cargo in multiple microtubules. In Section 3, we show the detail calculations of cargo-protein interactions. In Section 4, we show our simulation results of (1) the wall effect on a cargo transported by a single motor, and (2) the effective viscosity on a sphere being pushed through a cylinder containing a fluid with macromolecules. In Section 5, we show that large loads on the motor (when it is greatly extended) occur when the cargo is near the microtubule and far from the axon wall. In Section 6, we show how we analyzed the electron micrographs of axon cross sections to determine whether the distribution of microtubules is given by the Poisson distribution. In Section 7, we describe some ways to make our simulation more realistic.

1. Wall correction: Heuristic Approach

1.1 Effect on Translational Motion

Generally, the axoplasm has a viscosity that can be an order of magnitude larger than the viscosity of the water. The dynamical viscosity may be enhanced further due to the relative motion between the cargo and the axonal wall. In order to incorporate the wall effect quantitatively, let us consider translation of a spherical cargo of radius a moving in a cylindrical axon of radius R (Fig. 1 in main paper). We assume the viscosity of the axoplasm in an unbounded medium is η_0. Due to the finite size effect, the Stokes force experienced by the cargo moving with velocity $\boldsymbol{v}$ in the laboratory frame of reference is modified and can be expressed as in Eq. 1 in the main paper (1):

$$\boldsymbol{F} = 6\pi\eta_\infty a\boldsymbol{v}\, K(\boldsymbol{x}),$$

where $K(\boldsymbol{x})(\geq 1)$ is the correction factor due to the boundary wall effect and $\boldsymbol{x}$ is the position of the cargo. Here we assume the velocity of the cargo in the direction parallel to the axis of the axon tube. $K(\boldsymbol{x})$, in principle, depends on the position $\boldsymbol{x}$, the radius a of the cargo, and the diameter D of the axon.

The exact solution for the correction factor, $K(\boldsymbol{x})$, for a sphere moving along the axis of a cylinder filled with viscous fluid has been obtained numerically by solving a set of linear equations (1, 2).

Brenner and Happel, by employing the method of images, have given an asymptotic solution for a sphere positioned arbitrarily and eccentrically about the axis of the cylinder (3). However, those solutions are valid in the limit when the radius of the sphere is much smaller than to the size of the cylinder, and the sphere is not far from the axis. When the size of the sphere is comparable to that of the cylinder, Bungay and Brenner (4), and Tozeren (5) have provided approximate off-axis solutions perturbatively in terms of the eccentricity parameter that can be treated as small expansion coefficient,

$$\varepsilon = \frac{b}{R}$$

where b is the distance of the center of the sphere from the axis of the cylinder and R is the radius of the cylinder (Fig. 1 in main paper). All of the findings indicate that the viscous drag does not increase monotonically as ε increases. Instead, it reaches its minimum value around ε = 0.4, and then increases sharply afterwards. In fact this theoretical prediction has been verified experimentally in the optical feedback system and in circular conduits (6).

To the best of our knowledge, there is no converging general solution for $K(\boldsymbol{x})$ that applies over the entire range of possible positions and sizes of the sphere. For a rigid wall, the no-slip boundary condition dictates that the velocity of the sphere should tend to vanish when it approaches to the wall. This implies an infinite viscous drag and the functional behavior of the correction factor can be approximated as $K \sim 1/h$ for $h \to 0$, where h is the surface-to-surface distance of the sphere from the wall. By exploiting the behavior of the solutions near the axis and near the wall, we can heuristically write an approximate solution as a superposition, which is presumably valid over the entire range for 0 < ε < 1. Noting the fact that the off-axis viscous drag also depends upon the ratio of the radius of the sphere to the radius of the cylinder

$$k = \frac{a}{R},$$

Ambari (6) presented the experimental data for the correction term as a function of ε for different values of k. In order to fit these experimental data, we write the correction term in the form shown below and in Eq. 2 in the main text.

$$K = \exp(-k\varepsilon)\, K_0 + k^2\varepsilon^2\ f(\varepsilon)\,(R/h)$$

Here, K_0 is the wall correction factor for rigid spheres moving in a still liquid along the axis of a cylindrical tube (b = 0), and $f(\varepsilon)$ is an eccentricity function (1, 3), and h is the sphere-cylinder surface to surface distance. For the correction factor K_0, we use

$$K_0 = \frac{1 - 0.75857k^5}{1 - 2.1050k + 2.0865k^5 + 0.72603k^6}$$

When ε is near zero (i.e., the sphere is near the cylinder's axis), we make the approximation

$$f(\varepsilon) = 2.10444 - 0.6977\varepsilon^2$$

For values of ε near 1 (corresponding to a sphere near the cylinder wall), we use

$$f(\varepsilon) = \frac{9}{16(1-\varepsilon)}$$

It is evident that the heuristic correction recovers the previous results for both the limiting cases $\varepsilon \to 0$ and $h \to 0$. We have verified that our heuristic calculations are in agreement with the experimental results given by Ambari (6) as shown in Figure 1*C*.

In Fig. 1 in the main text, we show the correction factor *K* as a function of sphere-cylinder surface to surface distance *h* for two values of *k*, namely $k = 0.1$ and $k = 0.5$, where the radius of the sphere was fixed at $a = 250$ nm, and *k* was altered by changing the radius of the axon. The Faxén correction (1) for the sphere of the same radius moving parallel to a planar surface is also shown. The heuristic calculation also agrees well with the Faxén correction for a large cylinder with the sphere far away from the wall. Two general features of our results are of interest. First, relatively close to the wall, the boundary effect is very large, and second, for cargos that are relatively large with respect to the caliber of the axon (i.e. roughly filling it by half), the "wall" effect is evident even quite far away from the wall. For example, if we think of $\eta_{eff} = K\eta_{\infty}$ as an effective viscosity, then η_{eff} can be 50 times that of water for $K = 5$ and $\eta_{\infty} = 10$ times that of water (7). Previous theoretical findings indicate that viscous drag does not increase monotonically as ε increases. Instead, the minimum value is about $\varepsilon \approx 0.4$ and then the drag increases sharply with increasing ε (1); this prediction has been verified experimentally in an optical feedback system and in cylindrical conduits (6). We tested our phenomenological calculations against the experimentally measured correction factor (6) and found good agreement as shown in Fig. 1*C*.

1.2 Effect on Rotational Motion

The moving sphere approaching near the wall may also rotate due to the velocity gradient in the flow, and the corresponding torque is given by (1)

$$\boldsymbol{\tau}_{wall} = -8\pi\eta a^3 \boldsymbol{\omega},$$

where **ω** is the angular velocity of the rotation due to presence of the wall. This torque should not be confused with the torque exerted by external forces such as the pull of the motor or thermal kicks. Due to axial symmetry there is no wall effect producing the rotational motion for a sphere moving along the axis of the cylinder. Following Greenstein and Happel (8) the frictional torque within the first order approximation can be written as,

$$\boldsymbol{\tau}_{wall} = -8\pi\eta a^2 g(\varepsilon) k^2 \boldsymbol{v} \times \boldsymbol{z},$$

where **z** is the unit vector along the axis of the cylinder, and $g(\varepsilon)$ is the rotational eccentricity function that satisfies

$$(1-\varepsilon^2)g(\varepsilon) \ll 1.$$

For a typical cargo size (a = 250 nm) and motor velocity (v = 800 nm/s) and in a medium with the viscosity of water, one can estimate that the magnitude of the rotational torque is of the order of $\tau_{wall} \sim 1$ pN·nm. However, the torque experienced by a similar cargo driven by a kinesin motor with a load of 1 pN force is about 250 pN·nm. So we henceforth neglect the wall effect on the rotational motion.

2. Modeling of Kinesin Motors

In this paper we use the three-dimensional Monte Carlo method, as outlined in the Ref. (9), to study the transport carried out by kinesin motors(s). In this model, we consider kinesin molecules bound to a spherical cargo (vesicle), and the heads of the motor(s) are free to search for a place to bind on the protofilaments of the microtubule (MT). All places on the MT are available for binding. Once the motor head can reach the MT, we use a motor binding rate of 2 s^{-1}. It should be pointed out that the diffusion of the head was not incorporated into our model. The rule for the binding of the head to the microtubule was dictated by where the tail of the motor was attached to the surface of the cargo - that is, if the tail-microtubule distance was less than the native (unstretched) motor length, the motor bound to the MT at a given rate of 2 s^{-1} in our simulation. Nonetheless, we expected thermal fluctuations of the cargo to play a significant role in the motor(s) abilities to reach (and bind to) the microtubules.

We ignored head-head dynamics of a motor, and as others have done, simply modeled kinesin as a single head that hopped from one binding site to the next with step size of d = 8 nm, moving toward the plus end of the MT. We model kinesin as a monomer with a single head that can hop from one binding site to the adjacent site with a step size of d = 8 nm towards the positive end of the MT. These motors exert an elastic force on an object only when they are stretched, not when they are compressed. In our model, the tails of the motors are always bound to the cargo. Motors can actively participate in the cargo hauling process only when they are engaged, i.e., bound to the MT. In the presence of ATP molecules, the stochastic stepping of the motors is governed by Michaelis-Menten kinetics (10). The stepping of the motors applies mechanical force to the cargo. In our model, the tails of the kinesins were always bound to the cargo while the head could bind the MT. The motors participated in the transport process only when they were engaged, i.e., bound to the MT. In addition to the forces acting on the cargo due to the molecular motors and viscous drag, it also underwent Brownian motion.

2.1 Kinesin Kinetic Cycle and Stepping

In order to introduce our notation and parameters, we briefly review in this subsection how the kinesin completes its kinetic cycle and exerts mechanical force on the cargo.

Kinesin moves processively towards the plus end of the MT by hydrolyzing ATP molecules. The velocity of the movement of the kinesin is determined by the rate of binding of ATP to the motor head and its subsequent hydrolysis,

$$K + ATP \rightleftharpoons (K \cdot ATP) \rightarrow K + ADP + P_i$$

We denote motor-ATP on (binding) and off (unbinding) rates by k_{on} and k_{off}, and the rate of the ATP hydrolysis by k_{cat}. After hydrolysis of ATP, ADP and the phosphate ion P_i are released. The motor stepping velocity is given by the Michaelis-Menten rate of the chemical reaction (11):

$$V = \frac{V_{max}[ATP]}{[ATP] + K_m}$$

where [*ATP*] is the ATP concentration and V_{max} is the maximum velocity at the saturated concentration of the ATP molecules which can be expressed in terms of the load dependent efficiency function, $\zeta(F)$, as

$$V_{max} = k_{cat} d \zeta(F),$$

where *F* is the external load on the motor. The efficiency function, $\zeta(F)$, is maximum at zero load and decays to zero at the motor stall force. We therefore write the approximation

$$\zeta(F) = \left(1 - \left(\frac{F}{F_0}\right)^2\right).$$

The Michaelis-Menten constant K_m is defined by

$$K_m = \frac{k_{cat} + k_{off}}{k_{on}}.$$

The off-rate of ATP from the motor head, in principle, also depends upon the applied load *F,* and can be scaled in terms of experimentally measurable parameters as

$$k_{off} = k_{off}^0 \exp\left(\frac{F\delta}{k_B T}\right),$$

where $k_B T$ is the thermal energy, δ is a characteristic length, and k_{off}^0 is the no load off-rate that can be fitted with the experimental results (12).

The finite value of the run length during the stochastic stepping of the kinesin implies a finite lifetime of the motor-MT bound state. We follow the detachment kinetics as discussed in (11) in order to quantify the rate of dissociation of kinesin molecules from the MT. The probability of the detaching from the MT per unit time before ($P_{detach1}$) and after ($P_{detach2}$) the ATP binds are defined as

$$P_{detach1} = \frac{BP_{step}}{[ATP]},$$

$$P_{detach2} = \frac{\exp(\mathrm{F}\frac{\delta_l}{k_B T})P_{step}}{A},$$

where

$$P_{step} = \frac{k_{cat}\zeta(F)[ATP]}{[ATP]+K_m}.$$

Here, δ_l, A and B are physical constants characteristic of the molecular motor, and can be fitted with the experimental data (12). Once the detachment rates are known, the probabilities that the motors dissociate from the MT in each Monte Carlo time step dt are $P_{detach1}dt$ and $P_{detach2}dt$ before and after the ATP binds. The motor detachment rate above stall is, however, constant.

The list of constant parameter values used in our simulations is given in Table S1.

Table S1: Parameters and Values for the Motor Simulation

Parameters	Values	Comments
δ	1.3 nm	Characteristic length
d	8 nm	Step
k_{on}	2 μM s^{-1}	ATP on-rate
k_{off}^0	55 s^{-1}	ATP off-rate
k_{cat}	105 s^{-1}	Rate of hydrolysis
$[ATP]$	2000 μM	ATP concentration
A	107	Constant
B	0.029 μM	Constant
l	110 nm	Motor length
k	0.32 pN/nm	Motor spring constant
T	300 K	Temperature
dt	$10^{-6}-10^{-5}$ s	Time step
r_{MT}	12.5 nm	Radius of MT
k_{off} (back-detach)	2 s^{-1}	Above stall-detachment rate

2.2 Cargo Dynamics

In a viscous medium, a cargo under the action of molecular motor(s) undergoes diffusive-directive motion. It is capable of translation as well as rotation due to the resultant Brownian kicks from the molecules in the medium.

For a given axonal cross section and MT position, we assume that the head of the kinesin molecule can bind to the MT at time $t = 0$. If the motor state is on, there is a certain waiting time between the motor binding and the ATP hydrolysis plus ADP release. Once the ATP is hydrolyzed, the motor head instantly takes a step forward of $d = 8$ nm towards the plus end of the MT. As the head steps forward, the motor gets stretched and exerts mechanical force on the cargo. Since the motion is highly overdamped, the time to reach the Stokes regime is much smaller than any relevant time scale in the system. The dynamics of the cargo is modeled by the Langevin equation,

$$m\frac{d}{dt}\boldsymbol{v}(t) = -\alpha_T \boldsymbol{v}(t) + \boldsymbol{f}^{ext}(t) + \boldsymbol{f}^{thermal}(t).$$

The first term on the right hand side is the drag force at the instant when the cargo is moving with velocity $\boldsymbol{v}(t)$, and the drag coefficient is given by

$$\alpha_T = 6\pi K(\boldsymbol{x})\eta_0 a,$$

where the correction factor $K(\boldsymbol{x})$ is given by Eq. (2) in the main paper, and $\boldsymbol{x}$ is the position of the cargo with respect to the wall. The second term is the sum of all external forces due to motor(s) and the confining potential (if any). The last term is the sum of the all forces due to the erratic kicks given by fluid molecules that give the cargo Brownian motion.

If we assume that the cargo to be in a state of mechanical equilibrium, the average velocity is a time independent quantity and we can integrate the above equation in the presence of thermal fluctuations to obtain the time evolution of the position of the center of mass of the cargo (9):

$$\boldsymbol{x}(t+\Delta t) = \boldsymbol{x}(t) + \frac{\Delta t}{\alpha_T}\boldsymbol{f}^{ext}(x,t) + \sigma_T \boldsymbol{\varepsilon}_T,$$

where we have defined

$$\sigma_T = \sqrt{\frac{2k_B T \Delta t}{\alpha_T}},$$

and $\boldsymbol{\varepsilon}_T$ is a three-dimensional random variate drawn from a normally distributed function of zero mean and unit standard deviation. An analogous equation can also be derived for the torque and the rotational motion of the cargo. The details of the calculation can be found in Ref. (9).

Throughout our simulation, the motor-cargo system satisfies the following boundary conditions: (i) the motor cannot enter into the cargo or the MT; (ii) the cargo cannot enter into the MT; and (iii) the cargo must lie inside the axon.

2.3 Implementation of Multiple Motors on Multiple Microtubules

It has been shown both in vitro and in vivo that the effective transport of a comparatively large cargo is, basically, carried out by several molecular motors (13). The multiple-motor transport is particularly important in a geometrically constrained cell such as a neuron since the undulations and constrictions of a long narrow axon could obstruct the motion significantly.

For a given cargo size, axon caliber, and MT position, multiple motor transport depends upon how the motors are distributed over the surface of the cargo. It also depends upon the state of the motors. For instance, if the motors are uniformly distributed over the surface of the cargo and if their density is low, the transport is basically associated with a single motor since only one motor at a time can access the MT. Multiple motor transport is also influenced by the initial binding state and the attachment rate of the motors to the MT. The higher the motor binding rate, the longer is the run length of the cargo.

In our two-MT-multiple-motor simulations, we fix the position of 2 MTs parallel to the axis of the axon and let one of the motors bind to either of the MTs randomly. The binding process, position of the cargo and the size of the axon all satisfy the boundary conditions mentioned before. It should be noted that the initial motor state, i.e., whether the motor is on (ATP-bound) or off (ATP-unbound) also affects the transport properties. In the simulations, we assume an ATP molecule is bound to the head of the motor at the time when the motor attaches to the MT. When transport starts, only one motor is allowed to bind to the MT and the rest of the motors are free. Multiple motor transport along a single MT is discussed in detail in Ref. (9). Here we describe briefly the scenario of multiple-motor transport along two MTs (see Fig. S1).

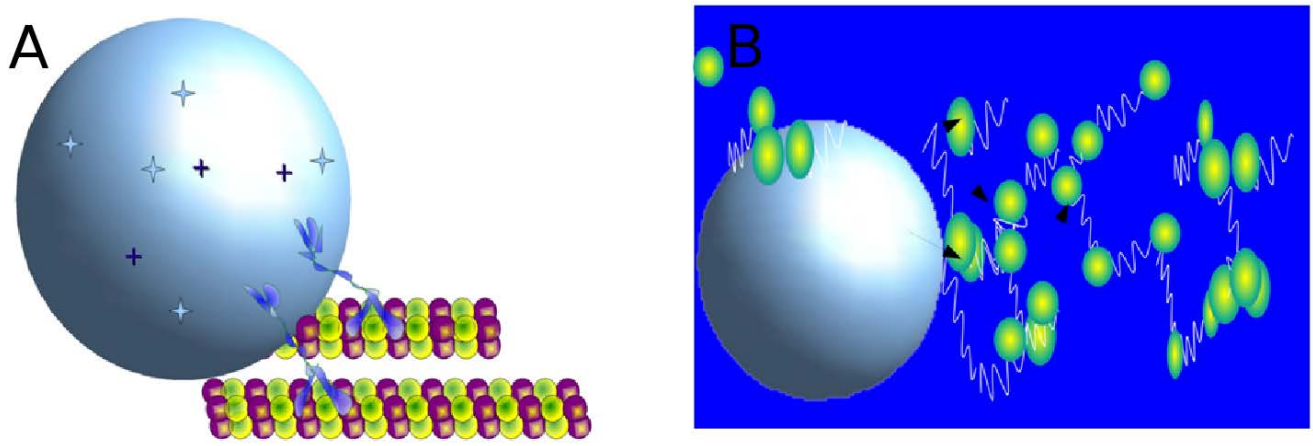

Figure S1: (*A*) A cartoon of a cargo being hauled by multiple motors along parallel microtubules. (*B*) Cargo interacting with polymers. A polymer is modeled by a chain of beads linked by tiny springs. Unlike the cargo, each bead of a polymer performs constrained diffusive motion.

Our simulation for the calculation of the run length goes as follows:

At $t = 0$, a given number of motors is specified.
A single motor is fixed at a point defined by spherical coordinate angles (θ, φ) on the surface of the cargo.
The tails of rest of the motors are distributed in a region from (θ, φ) to $(\theta + 0.01\pi, \varphi + 0.01\pi)$.
In other words, the tails of the motors are clustered together on the surface of the cargo.
At $t = 0$, a single motor is allowed to bind to one of the MTs to initiate the simulation.
At $t > 0$, the motors that can reach to the MT will be able to bind without bias at the binding rate of 2 per sec.

The binding of the motors to the second MT depends upon the MT's position. If a motor can reach both the MTs at the same time, then there is a 50/50 chance of binding. This means the motor tries to bind to the first MT. If it fails, then it tries to bind to the second MT. In both cases, the binding rate of a motor to a MT is still 2 s^{-1}.
In the course of time, motors can bind and unbind from the MTs as well as switch back and forth between the MTs. The binding, unbinding, and stepping processes of the motors are governed by Micheles-Menten detachment kinetics.

The state of the cargo is defined by the states of the motors. Basically the cargo can be hauled along one or two MTs, depending upon the state of motors. In principle, when the motors can reach both the MTs, this allows the cargo to straddle both MTs when the separation between the MTs is less than twice the native length of the motor.

The run length of the cargo is defined by the total mean distance travelled by the center of mass of the cargo without dissociating from the MT(s). In the simulation, we do not consider the direct motor-motor interactions. However, motors can interact via their forces on the cargo.

3. Effect of Macromolecules Crowding the Cargo

The biological medium differs greatly from an idealized system due to large molecules in the cytoplasm. In particular, in a neuron, owing to the confined geometry of the axon, the effective cargo-protein interactions may be much more pronounced than in an ordinary cell. Axoplasm consists of an abundance of large molecules such as microtubule-associated proteins (MAPs) bound to microtubules (14, 15), the C-termini of neurofilaments medium and heavy with long side arms (15-17), and plectin 1c (18) which is a member of a family of cytoskeletal linking proteins (19).

3.1 Cargo-Protein interaction

3.1.1 Spring-Bead Model

The detail molecular structure and dynamics of the residues of these large molecules using microscopic modeling such as molecular dynamics is computationally challenging and time demanding. In order to get a rough estimate of how a crowded environment affects the cargo dynamics in a confined geometry, we model the cargo-protein interactions by considering each polymer as a chain of spherical beads coupled by massless springs. The motion of each polymer consists of the motion of its constituent beads, each of which diffuses in a constrained environment. In a dense medium, we also incorporate the protein-protein interactions via bead-bead collisions. We assume the interaction is attractive when the beads are far apart and repulsive when they are very close together (at very short range); the interaction is the standard Lennard-Jones (LJ) potential. The LJ potential is useful to model the interaction between particles at the atomic level (20):

$$V_{LJ} = 4\varepsilon\left[\left(\frac{\sigma}{r}\right)^{12} - \left(\frac{\sigma}{r}\right)^{6}\right]$$

The LJ parameters ε and σ are the potential depth and the equilibrium distance of the interparticle separation. r is the distance between the 2 particles. In our simulation, the potential does not enter into the calculation explicitly. We define the forces on the cargo due to polymers, $\boldsymbol{F}_c$, and on the i^{th} bead due to other beads, $\boldsymbol{F}_i$, as the sum of the forces

$$\vec{F}_c = -\sum_{j=1}^{N} \frac{\partial V_{LJ}(c, j)}{\partial r}\hat{r}$$

$$\vec{F}_i = -\sum_{j\neq i}^{N}\left(\frac{\partial V_{LJ}(i, j)}{\partial r}\right)\hat{r} - k_s\left(\vec{x}_{i+1} - \vec{x}_{i-1}\right)$$

where the sum, in principle, runs over all beads, N is the total number of beads, and $\hat{\boldsymbol{r}}$ is a unit vector. The spring constant k_s is defined as

$$k_s = \begin{cases} k & \boldsymbol{x}_{i+1}, \boldsymbol{x}_{i-1} \in \text{same polymer} \\ 0 & \text{otherwise} \end{cases}$$

Each bead and the cargo perform Brownian dynamics with an additional force originating from the interactions, i.e., the positions of the bead and the cargo at any given time are calculated according to

$$\boldsymbol{x}_i(t+\Delta t) = \boldsymbol{x}_i(t) + \frac{\Delta t}{\alpha_T(i)}\boldsymbol{F}_i + \sigma_T(i)\boldsymbol{\varepsilon}_T,$$

$$\boldsymbol{x}_c(t+\Delta t) = \boldsymbol{x}_c(t) + \frac{\Delta t}{\alpha_T(c)}\boldsymbol{F}_c + \sigma_T(c)\boldsymbol{\varepsilon}_T,$$

where the thermal fluctuation coefficients $\sigma_T(i)$ and $\sigma_T(c)$ for the beads and the cargo can be different due to differences in their radii. While the cargo can perform free diffusion, the motion of the beads of each polymer is constrained due to the coupling to the neighboring beads via springs. In order to speed up the simulation, we have also introduced a cut-off in the potential, and the subsequent correction in the derivatives is added into the calculation in order to avoid the divergence in the spatial derivatives that come from the abrupt cut-off. In all our calculations, the cut-off distance is defined in terms of σ, the equilibrium distance of the LJ potential.

The parameter values for the cargo-bead simulations are listed in Table S2.

Table S2: Cargo-Protein Interaction Parameters and Values

Parameters	**Values**	**Comments**
η_0	10 η_w	η_w : viscosity of water
r_b	10 nm	Bead size
σ_b	1.12(2 r_b)	Bead equilibrium distance
σ_c	1.12(a+2 r_b)	Cargo-bead equilibrium distance
ε	1	Potential depth
L_z	1.6 μm	Length of the cylinder
k_s	2 pN/nm	Spring constant

3.1.2 Boundary Condition and Wall Effect

In order to find the mobility and effective viscosity in our simulations, we consider a cylindrical tube of diameter D, and longitudinal dimension L_z, filled with a medium of viscosity η_0. The volume concentration C of the polymers is defined by the ratio

$$C = \frac{V_p}{V_t}$$

where V_p and V_t are the net volume occupied by the polymers and the volume of the tube, respectively. The spherical cargo has radius a. At $t = 0$, we place the cargo at a distance $L_z / 4$ along the axis of the tube and apply an external force F so that it can move in the z-direction. (The cargo is not being hauled along the microtubule by motors; it is being driven by the external force F.) We end the simulation when the cargo reaches the point $3L_z / 4$. We record the time for the net displacement of $L_z / 2$. During this time the cargo as well as polymers can interact with their surroundings and can also experience the resistance from the wall. The wall effect for both cargo and the polymers is incorporated by rescaling the viscosity $\eta \to \eta_{eff} = K(\boldsymbol{x})\eta_0$ during the diffusion process.

3.1.3 Cargo Mobility and effective viscosity

When the cargo interacts with the beads in a polymer, it recoils due to Newton's third law. The recoil velocity of the cargo is much smaller than that of the bead due to a large cargo-bead size ratio. This effect can be significant if the polymer concentration is high.

In order to quantify the effect of the polymer-cargo interactions, we define cargo mobility μ and size-dependent effective viscosity η_{eff} as follows:

$$\mu = \frac{|\boldsymbol{v}|}{|\boldsymbol{F}|},$$

$$\eta_{eff} = \frac{|\boldsymbol{F}|}{6\pi a |\boldsymbol{v}|},$$

where $\boldsymbol{F}$ is the cargo driving force, a is the cargo radius, and $\boldsymbol{v}$ is the average velocity. The effective viscosity can also be found directly by using Stokes' formula:

$$\frac{\eta_{eff}}{\eta_0} = \frac{|\boldsymbol{v}|}{|\boldsymbol{v}_0|}$$

The average velocity in our simulation is calculated by measuring the average time for the cargo to travel through a given distance. We assume that the crowding and confinement renormalize the effective viscosity of the medium. This viscosity changes with the size of the cargo, the length and the density of the polymers, and the strength of the lateral confinement, i.e., the axonal caliber.

4. Results

4.1 Wall effect on transport by a single motor

We first explored how the wall would modify axonal transport of a cargo hauled by a single kinesin motor. We modeled the axon as a long cylinder of uniform diameter with a microtubule centered along the axis of the axon. (In practice, electron micrograph images (21) show a wide variation both in the caliber size and longitudinal undulation.) We investigated the magnitude of the wall effect on cargo motion via our simulations (Fig. S2), and consistent with the analytic results in Fig. 1, observed that the importance of the wall depended very much on the size of the cargo relative to the axon. For a D = 1200 nm axon with η_∞ = 10 times that of water, and with the 500 nm diameter cargo, the average load on the motor during the simulation was approximately 0.84 pN; the effect of such a load in our simulations in the presence of Brownian motion was consistent with past experimental results (11) and previous force-processivity data (11). Thus, for some parameter values, the effect of the increased drag due to the wall effect can be enough to decrease by approximately 50% the expected mean travel distance of a cargo that is hauled by a single motor. Such an effect would likely not be insignificant from a physiological point of view, since recent work (22) suggests that a roughly 25% decrease in motor processivity is enough to have significant consequences. Note that the parameters for the large cargo/small axon case considered are not unreasonable, since mitochondria are frequently on the order of 200 nm in diameter (23), and there are numerous axons on the order of 1 μm in diameter.

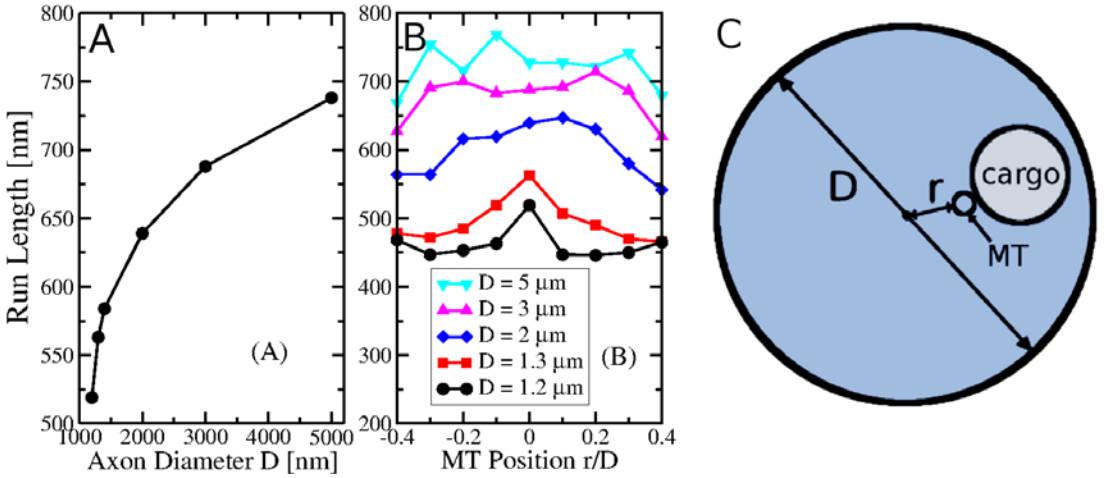

FIGURE S2 (*A*) Run length of a single motor hauling a cargo of radius a = 250 nm as a function of axon diameter when the microtubule (MT) is along the axis of the axon. The expected value of the run length of a cargo in water hauled by a kinesin molecule without any wall is about 800 nm **(24)**. In our simulation, the viscosity of the medium is 10 times that of the water **(7)** and the run length asymptotically approaches the unbounded value when the axon diameter approaches infinity. (*B*) Run length of a cargo hauled by a single motor versus the scaled distance r/D of the microtubule from the axis of the axon for different axon diameters D. r is the distance of the center of the MT from the center of the axon. The MT is parallel to the axis of the axon. The position of the MT with respect to the diameter D of the axon has been rescaled so that all data fits in a single plot. For large axons, the run

lengths fairly remain constant except when the MT is close to the wall. For small caliber axons, the run length increases slightly when the MT is along the axon axis. Here each data point is the average of 1000 runs. (*C*) Cartoon depicting cross section of axon of diameter *D* with MT center a distance *r* from the axon center, and the cargo touching the MT.

4.2 Potential effect of crowding

The biological medium differs from an idealized Newtonian fluid, in part due to large molecules or parts of large molecules that can impede cargo motion due to steric hindrance. To investigate theoretically how large molecules could hinder cargo transport through such effects, we included polymers in our simulations as described in the Methods section.

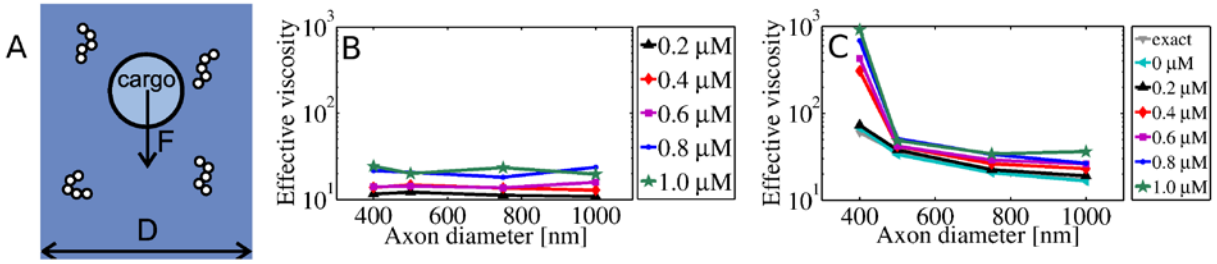

FIGURE S3 (*A*) Cartoon depicting the simulation used to calculate the effective viscosity. A sphere subjected to a constant force *F* moves through a cylinder of diameter *D* containing a fluid with polymers. (*B*) Effective viscosity of the medium in the presence of 200 nm long polymer chains consisting of 10 beads, each with 20 nm diameter as a function of axon diameter D *without* the wall effect (correction factor K=1 in Eq. 2). In the absence of the enhanced viscosity near the wall, the caliber size of the axon does not have any noticeable effect. (*C*) Effective viscosity *with* the wall effect. For comparison, the exact viscosity for a cargo moving along the axis given by Haberman and Sayre (1, 2) is also shown at 0% polymer concentration. Note that the concentration of the polymers enhances the viscosity significantly. This enhancement is very pronounced for small caliber axon when the wall effect is incorporated. Here the radius of the cargo is a = 100 nm and the length of the polymer is set at L = 200 nm. The concentration in μM refers to the number of micromoles of polymer per liter.

Obviously, the higher the polymer concentration, the more effect it had. Thus, we investigated the effect of macromolecules in the axoplasm on the effective viscosity for concentrations of 0, 0.2, 0.4, 0.6, 0.8, and 1.0 μM, corresponding to approximate excluded volumes of 0%, 0.5%, 1%, 1.5%, 2%, and 2.5%. To keep the polymer concentration constant for different caliber axons, we varied the number of polymers as we varied the axon diameter. Each polymer was modeled by a chain containing between 10 beads, each of radius 10 nm coupled through a tiny spring with spring constant 2.0 pN/nm. Because many axonal cargos are small, the cargo radius was fixed at 100 nm, while the diameter of the axon (tube) was varied from 400 nm to 1000 nm. Both the viscosity and mobility data show a clear deviation from the free transport values due to cargo-polymer interactions and the wall effect.

In Fig. S3, we separate the effect of confinement and of crowding by the polymers on the cargo mobility (quantified in terms of effective viscosity) for different polymer concentrations. In Fig. S3*B*, we show the effect of the presence of polymers alone, without incorporating the wall effect on the polymer

filaments and on the cargo. There was a significant enhancement of the "base" viscosity of the medium as the concentration of the polymer increased. This enhancement came from the excluded volume effect. When the wall effect was included (see Fig. S3*C*), the effective viscosity remained fairly constant for a given volume exclusion (polymer concentration) in large diameter axons. However, the wall effect became important and was the dominant factor inhibiting cargo mobility as the caliber size decreased, and the presence of the polymers increased the wall effect. The length scales for which the wall effect became important are discussed next.

4.3 Onset of the wall effect when the cargo radius and cargo-wall distance are comparable

Noting that the presence of long molecules dramatically enhanced the opposition to the motion for even a relatively small cargo in a small caliber axon, we wanted to better understand how the onset of huge resistance depended on the different length scales of the system. The explicit lengths involved in the system were the radius of the cargo (a), the diameter of the axon caliber (D), and the length of the polymers (L), and the distance of the surface of the cargo to the inner wall of the axon (h).

For a Newtonian fluid, the mobility of a spherical object is inversely proportional to its size, while the coefficient of viscosity is the property of the medium, and is size independent. Cytosol, especially the axoplasm, is a complex fluid with large molecules, and is expected to be a non-Newtonian fluid, i.e., the mobility and thus the effective viscosity should vary with the size of the object. In our simulation, as indicated above, we modeled each polymer chain as a system of beads coupled by tiny springs. The size and the number of beads determined the net volume exclusion. We varied the length of the polymer by changing the number of beads linked together while keeping the overall density of the beads (excluded volume) constant. We also varied the size of the cargo as well as the diameter of the axon.

For a small caliber axon, when thermal fluctuations pushed the cargo away from the axonal axis, the average cargo-wall distance, h, could be comparable to the polymer length. In that case one might expect strong cargo-wall coupling via the polymers, leading to a large resistance to cargo transport. However, we observed a very weak dependence on the length of the polymer, as long as the volume exclusion remained constant (see the Supporting Materal), suggesting that such direct cargo-wall coupling via filaments was not a dominant effect.

For a given polymer concentration (volume exclusion), however, the wall effect was significantly amplified by the presence of the polymer when the cargo was relatively close to the wall. In Fig. S3, we see that the wall effect for a given polymer concentration with a small cargo was fairly constant for large caliber axons: its effect was noticable only when the axon diameter was reduced to about D = 400 nm. Here, the cargo radius was 100 nm, so the corresponding ratio of h (distance of cargo surface to the wall) divided by a (cargo radius) was h/a = 1. We investigated whether the observed onset of a dramatic enhancement of the effective viscosity (or the reduction of the mobility) seen in Fig. S3 occurred more generally for cargos of other sizes, at around the same value h/a = 1 (Fig. 2). We observed that it did, for all polymer concentrations and for all polymer lengths; the presence of long molecules increased the 'base' viscosity of the axoplasm, which then resulted in amplifying the magnitude of the wall effect.

To understand whether the ratio h/a was a truly universal quantity, we varied the cargo size for different axon diameters in the regime where $h/a \approx 1$ for a concentration of polymers equal to 4.17% excluded volume. These concentrations were 16.5 μM, 3.31 μM, and 0.827 μM for polymers of lengths 20 nm,

100 nm, and 400 nm, with beads of radius 10 nm. In Fig. 2, we show the extracted effective viscosity data for different calibers and cargo radii expressed in terms of the parameter h/a. It is interesting to note that, irrespective of the axon or cargo size, the effective viscosity dramatically increased when $h/a \leq 1$ for all axon and cargo dimensions. Physically, small h meant that the cargo was close to the wall, and large a meant that there was a large amount of cargo surface area to enhance the viscous drag produced by proximity to the wall of the axon. Thus the wall effect became insignificant if the cargo-axon geometry satisfied the condition $h/a \gg 1$.

5. Relation between the load on the motor and the location of the microtubule

The cargo is subjected to a greatly enhanced viscosity when it is very close to the wall of the axon. For this reason, it avoids the wall. Suppose the cargo is close to the wall of the axon. As the motor walks along the MT and pulls on the cargo, the wall exerts a drag force parallel to the wall and the MT. This force stretches the motor. The component of the force perpendicular to the wall and the MT pushes the cargo down toward the MT. In our simulations we find that the cargo avoids being close to the wall. In Figure S4*A*, we plot the run length vs. load on the motor at the time when the motor detaches from the MT for a large and small diameter axon. The load on the motor is given by the amount that the motor is stretched multiplied by the spring constant of the motor. For small loads, the average run length (travel distance) is about the same for both axon sizes. However, for large loads (greater than 8 pN), the run length is considerably shorter for the smaller caliber axon. Figures S4*B* and S4*C* show that the large loads on the motor occur when the cargo is near the microtubule and far from the axon wall. The reduced run length in the small caliber axon is due to the viscosity that is enhanced by the small diameter of the axon. The nominal viscosity of the axoplasm in our simulations is 10 times that of water. With the correction factor (Figure 1 in main paper) of 5 far from the wall, the effective viscosity is about 50 times that of water.

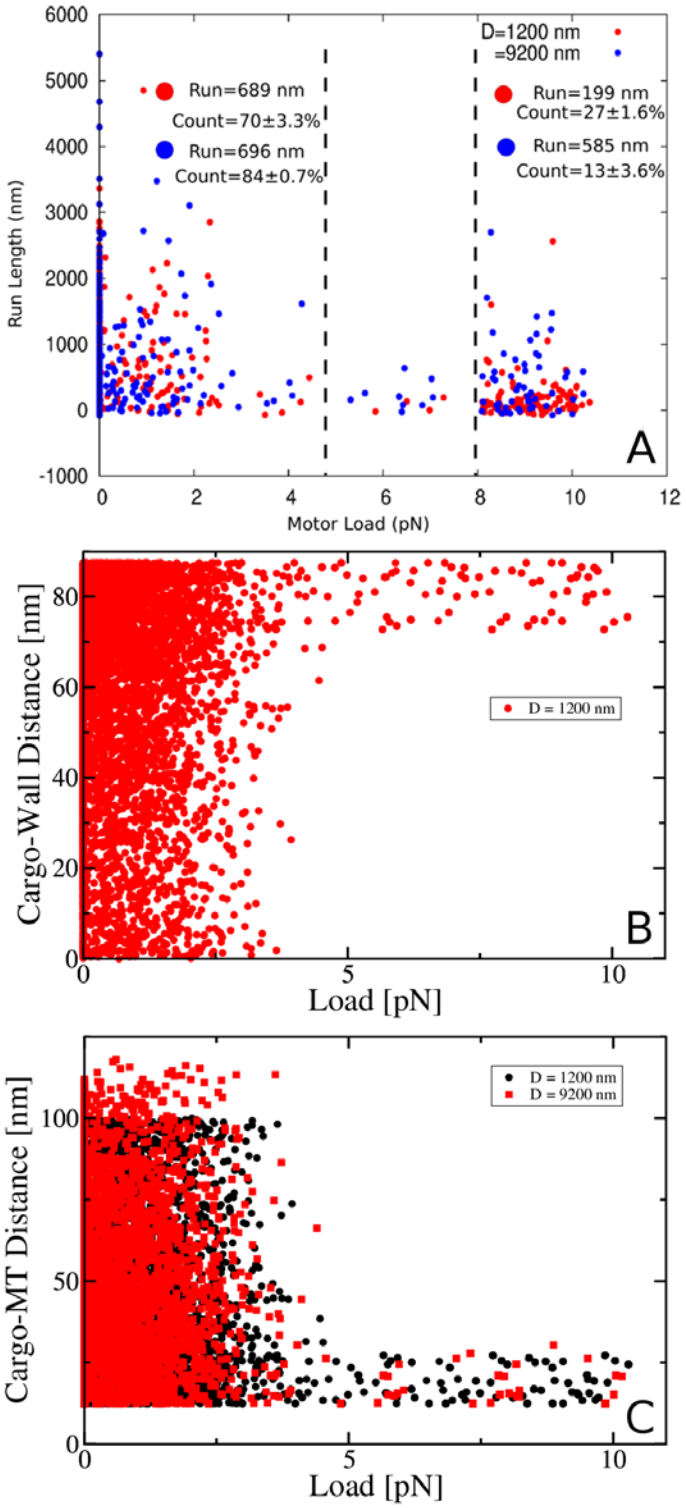

Figure S4: In all of these scatter plots, a single motor hauls a spherical cargo with a radius of 250 nm along a single microtubule centered on the axis of the axon. We show two axon diameters: 1200 nm and 9200 nm. Each point represents a single run. (*A*) Run length versus the load on the motor at the time when the motor detached from the microtubule. The run length is shorter for high loads (> 8 pN) in the

smaller axon. Data is from 400 runs. (*B*) The distance between the inner wall of the axon and the surface of the cargo versus the load on the motor when it detached. (*C*) The distance between surface of the cargo and the surface of the microtubule versus the load on the motor when it detached. Notice that the motor can have a large load when it is near the microtubule, but never when it is near the wall and hence far from the microtubule.

6. Electron Micrograph Images of Axons and Their Microtubule Distribution

Here we present some examples of electron micrograph (EM) images of small caliber axons where we have measured the distribution of microtubules. Electron micrograph images of axonal cross section of small and large motor neurons of mice were analyzed by paying particular attention to the microtubule distributions. In some EMs, the resolution or magnification were such that it was hard to identify microtubules, so those images with indistinguishable microtubules were discarded. To determine whether the microtubules were randomly distributed or not, we overlaid a grid onto the images such that there was an average of roughly one microtubule per grid square. We then counted the number of visible microtubules in each square that was fully contained within the axon's boundary (25). The grid size was such that there was approximately one MT per square, i.e., the side of a grid square ranged from 0.2 to 1 μm. An example is shown in Figure S5. Given the mean number of microtubules per square, we could then use the Poisson distribution with that mean to calculate the probability of finding a given number of microtubules in a square. Values of chi-squared (representing the deviation of the results from the Poisson distribution) and *p* (the probability that the microtubules were randomly distributed) were then calculated. In most cases we found that the MTs were randomly distributed and agreed well with a Poisson distribution (Fig. S5*C*). Of the nine images with readily visible microtubules, eight had p-values greater than 0.05, suggesting microtubules were largely randomly distributed (Figure S5). In some axons the MTs appear to be clustered (see Figure S6) and we find the MTs in a cluster tend to be within 100 nm of each other as long as the overall MT density is comparable to that of similar caliber axons. Figure S6 had a *p*-value below 0.05, suggesting a nonrandom clustering of microtubules. Of course, one axon is not enough to draw any conclusions about whether the microtubule arrangement is random or not; this one axon could simply be one of the rare axons whose arrangement of microtubules puts it in the tail of the Poisson distribution. However, previous work has also found microtubule bundling in axons (16, 26, 27). A summary of the axonal EMs that we examined is shown in Figure S7 where we plot the p-value vs. the MT density of the axon in Figure S7*A* and the *p*-value vs. the cross sectional area of the axon in Figure S7B. The *p*-value represents the probability that the distribution of MTs followed a Poisson distribution. Since a small *p*-value corresponds to a non-random distribution of MTs, we can see that most of the axons had a large *p*-value and thus, a Poisson distribution of MTs, regardless of the axon size, i.e., the axonal cross sectional area.

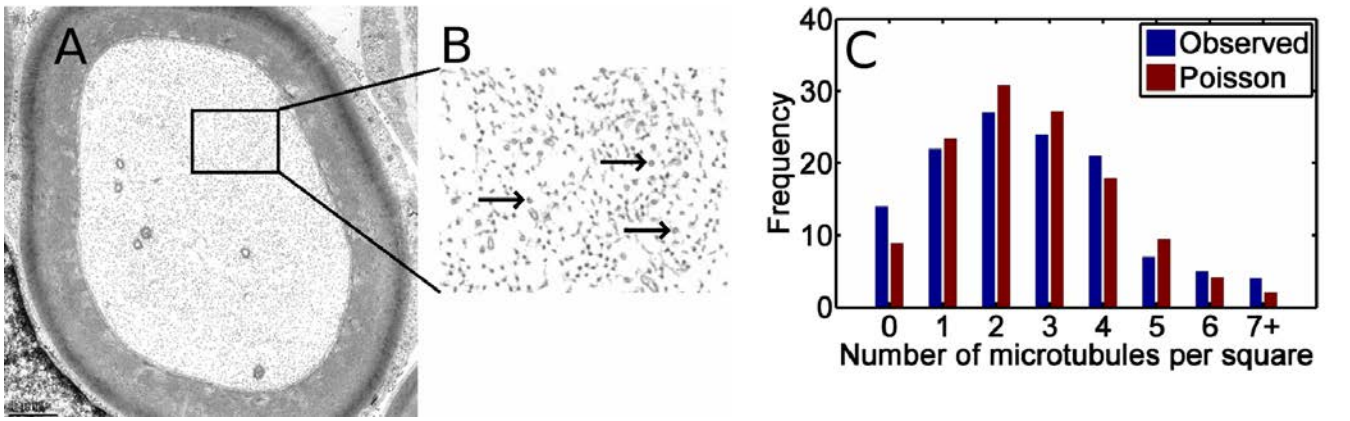

Figure S5. (*A*) Electron Micrograph (EM) image of the cross section of a myelinated axon of a large motor neuron of a 6-month-old mouse. The average inner diameter (excluding myelin) is about 6 microns. The MT density is 28.3 MTs/μm^2. (*B*) A zoomed portion of the cross section. Three arrows point out microtubules. Other microtubules are clearly visible. (*C*) Histogram comparing the observed distribution microtubules with the Poisson distribution (Poisson mean = 2.6371 MT/square). Good agreement with the Poisson distribution indicates that the MTs are randomly distributed. The *p*-value for a Poisson distribution of MTs is 0.5 in this case. The EM was analyzed by overlaying a square grid on the axon and counting the number of microtubules in each square. The mesh size was such that there was approximately 1 MT per grid square.

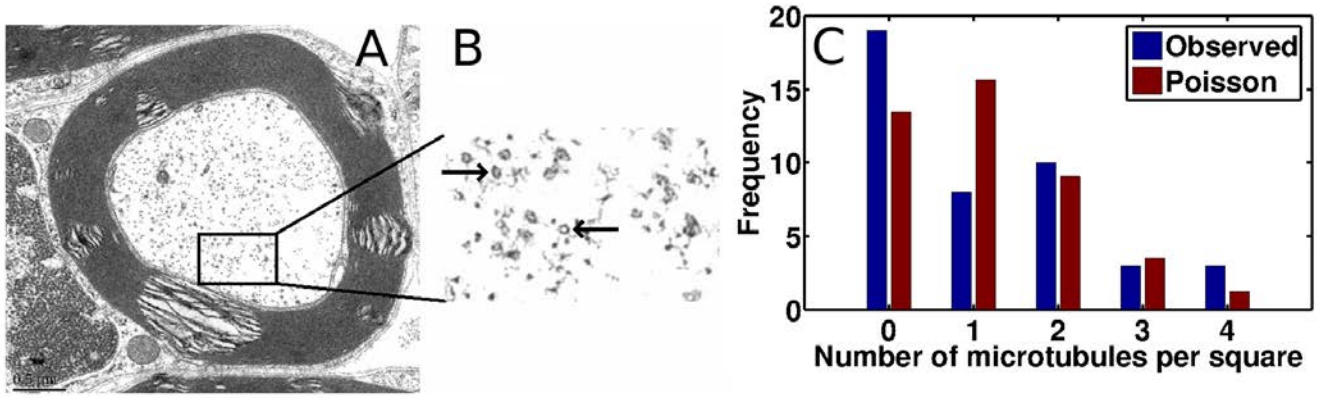

Figure S6. (*A*) Electron Micrograph (EM) image of the cross section of a myelinated axon of a small motor neuron of a 6-month old mouse. The average inner diameter (excluding myelin) is about 2.08 micron. The MT density is 3.2 MTs/μm^2. (*B*) A zoomed portion of the cross section. Two arrows point out microtubules. Other microtubules are clearly visible. (*C*) Histogram comparing the observed distribution microtubules with the Poisson distribution (Poisson mean = 0.9143 MT/square). Analysis was the same as in Figure S5. Poor fit to Poisson distribution indicates that the MTs were clustered. The *p*-value for a Poisson distribution of MTs is 0.035 in this case. However, since this is just one axon, one cannot draw any definite conclusions about whether the microtubule arrangement is random or not; this axon could simply be one of the rare axons whose arrangement of microtubules occurs 3.5% of the time in a Poisson distribution.

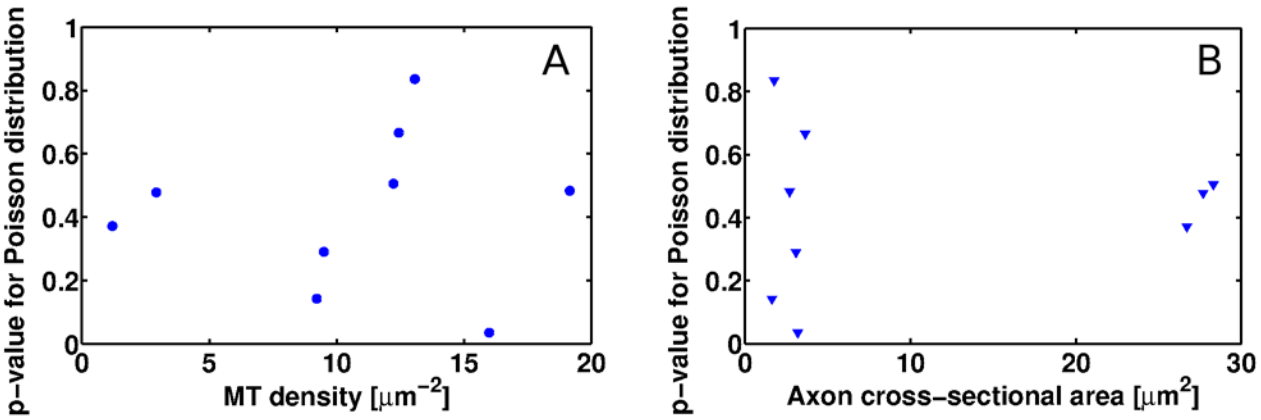

Figure S7. (*A*) *P*-value of Poisson distribution of microtubules versus the MT density. Each point represents the MTs in one axon. Low *p*-value indicates that the MTs are clustered and not randomly distributed. High *p*-value means that the MTs are distributed randomly according to a Poisson distribution. (B) *P*-value of Poisson distribution versus the cross-sectional area of the axon. Note that most of the axons have a random distribution of MTs, regardless of their size (cross-sectional area).

If the microtubules are randomly distributed, we can calculate likely nearest-neighbor distances given the average microtubule density. Given an average MT density ρ, the probability P that some MT will have a nearest neighbor within a distance r is (28):

$$P = 1 - e^{-\rho\pi r^2}$$

(Note that this expression goes to zero as r goes to zero, and to 1 as r goes to infinity; it increases with ρ.) Solve for ρ:

$$\rho = \frac{-\ln(1-P)}{\pi r^2}$$

We plot this equation in Figure 5 in the main text. A center-to-center distance of 75 nm between adjacent microtubules is more than sufficient for a single motor within range of the MTs to reach either of them, as discussed in the main text. If we set r to 75 nm, we can calculate values of ρ for different desired values of P as shown in Table S3.

Table S3: Microtubule Densities Needed For Various Nearest-Neighbor Probabilities at 75 and 200 nm

P (neighbor within distance)	ρ (MTs / μm^2), 75 nm	ρ (MTs / μm^2), 200 nm
0.75	78.45	11.03
0.8	91.08	12.81
0.9	130.3	18.32
0.95	169.5	23.84
0.99	260.6	36.65

Smaller-caliber axons have recorded microtubule densities of roughly 150 microtubules/μm^2, meaning a microtubule has a greater than 90% chance of having a neighbor within 75 nm. As mentioned above, some axons do appear to exhibit clustering in microtubules rather than random distribution; in these cases, the closest neighbors in a cluster are well within 75 nm.

For contrast, we also include the microtubule densities necessary for a microtubule to have a neighbor within 200 nm, although a separation this great makes multiple-microtubule transport unlikely. In the images of larger axons with the most clearly visible microtubules, microtubule densities ranged from roughly 12-25 microtubules/μm^2, corresponding to at least a 75% chance of any given microtubule having a neighbor within 200 nm.

7. More realistic modeling of axonal transport

The purpose of this paper has been to point out that there can be significant viscous drag on cargos moving close to the axonal wall, which effectively acts as a rigid wall. We have used a simple model of axonal transport to illustrate this, but there are clearly ways in which the model of axonal transport could be made more realistic. For example, we have modeled the cargo as a rigid sphere, but a variety of cargos with different shapes undergo fast axonal transport, e.g., membranous organelles and tubules, mitochondria, vesicles containing neurotransmitters, lysosomes, etc. (29). Some of these cargos could be deformed as they pass near the axon wall or near other cargos. In addition, we have modeled axoplasm as an isotropic viscous fluid containing polymers, even though it is a complex anisotropic heterogeneous viscoelastic fluid (30) containing polymers, and membranous organelles and tubules largely oriented along the axis of the axon. One way to model the axoplasm would be with the Burger's model which involves elastic moduli and viscous coefficients a circuit-type arrangement (30). In addition to the viscosity enhancement near the wall of the axon, the membranous tubules, e.g., the endoplasmic reticulum, in the axoplasm could also enhance the viscosity experienced by nearby cargos. This enhancement is not seen in nonneuronal cells as found in experiments where a reduction in the number of motors hauling lipid droplet in *Drosophila* embryos did not reduce the run length or the velocities of the cargo (13). Thus, it appears that at least without a nearby bounding membrane, intracellular membranes do not impair intracellular transport in nonneuronal cells because the vesicles are able to avoid close approaches where the viscosity is greatly enhanced. However, avoiding such close

encounters is not always possible in the confined geometry of the axon. This would explain why, as we mentioned above, inhibition of force generation by dynein arrested the motion of large lysosomes/late endosomes in axonal transport but had little effect on the transport of small vesicles (22). To model transport in the axon in the presence of membranous tubules is difficult because it requires too many unconstrained parameters such as the tubules' size, shape, location, and whether they are tethered or free floating. However, we believe that cargo transport via motors walking along two MTs simultaneously could be especially helpful in small caliber axons where pushing such membranous tubules out of the way is difficult because of the confined geometry. In addition, interactions between cargos traveling in opposite directions could also impair cargo transport, e.g., the organelle traffic jams (31, 32) that we mentioned above, but modeling this is well beyond the scope of this paper which just considers single cargo transport. Although our modeling suggests that small cargos like synaptic vesicles (~100 nm) can be transported in an axon without significant resistance, other larger cargos like mitochondria and lysosomes (22) may have more difficulties, especially in small caliber axons. This work thus provides a useful conceptual framework for such effects but the extent to which such scenarios contribute to disease progression in the animal remains to be explored experimentally.

SUPPORTING REFERENCES

1. Happel, J., and H. Brenner. 1965. Low Reynolds Number Hydrodynamics, With Special Applications to Particulate Media. Prentice-Hall, Englewood Cliffs, NJ.
2. Haberman, W. L., and R. M. Sayre. 1958. Motion of rigid and fluid spheres in stationary and moving liquids inside cylindrical tubes. In David Taylor Model Basin Report (no. 1143). Department of the United States Navy.
3. Brenner, H., and J. Happel. 1958. Slow viscous flow past a sphere in a cylindrical tube. *J Fluid Mech* 4:195-213.
4. Bungay, P. M., and H. Brenner. 1973. The Motion of a Closely-Fitting Sphere in a Fluid-Filled Tube. *International Journal of Multiphase Flow* 1:25-56.
5. Tozeren, H. 1982. Torque on eccentric spheres flowing in tubes. *J Appl Mech-T Asme* 49:279-283.
6. Ambari, A., B. Gauthier-Manuel, and E. Guyon. 1984. Wall effects on a sphere translating at constant velocity. *J Fluid Mech* 149:235-253.
7. Haak, R. A., F. W. Kleinhans, and S. Ochs. 1976. The viscosity of mammalian nerve axoplasm measured by electron spin resonance. *J. Physiol.* 263:115-137.
8. Greenstein, T., and J. Happel. 1968. Theoretical study of the slow motion of a sphere and a fluid in a cylindrical tube. *J Fluid Mech* 34:705-710.
9. Erickson, R. P., Z. Jia, S. P. Gross, and C. C. Yu. 2011. How molecular motors are arranged on a cargo is important for vesicular transport. *PLoS Comput. Biol.* 7:e1002032.
10. Visscher, K., M. J. Schnitzer, and S. M. Block. 1999. Single kinesin molecules studied with a molecular force clamp. *Nature* 400:184-189.
11. Kunwar, A., M. Vershinin, J. Xu, and S. P. Gross. 2008. Stepping, strain gating, and an unexpected force-velocity curve for multiple-motor-based transport. *Curr. Biol.* 18:1173-1183.
12. Block, S. M., L. S. Goldstein, and B. J. Schnapp. 1990. Bead movement by single kinesin molecules studied with optical tweezers. *Nature* 348:348-352.
13. Shubeita, G. T., S. L. Tran, J. Xu, M. Vershinin, S. Cermelli, S. L. Cotton, M. A. Welte, and S. P. Gross. 2008. Consequences of motor copy number on the intracellular transport of kinesin-1-driven lipid droplets. *Cell* 135:1098-1107.

14. Voter, W. A., and H. P. Erickson. 1982. Electron microscopy of MAP 2 (microtubule-associated protein 2). *J. Ultrastruct. Res.* 80:374-382.
15. Mukhopadhyay, R., S. Kumar, and J. H. Hoh. 2004. Molecular mechanisms for organizing the neuronal cytoskeleton. *BioEssays : news and reviews in molecular, cellular and developmental biology* 26:1017-1025.
16. Hirokawa, N. 1982. Cross-linker system between neurofilaments, microtubules, and membranous organelles in frog axons revealed by the quick-freeze, deep-etching method. *J. Cell Biol.* 94:129-142.
17. Hirokawa, N., S. Hisanaga, and Y. Shiomura. 1988. MAP2 is a component of crossbridges between microtubules and neurofilaments in the neuronal cytoskeleton: quick-freeze, deep-etch immunoelectron microscopy and reconstitution studies. *J. Neurosci.* 8:2769-2779.
18. Fuchs, P., M. Zorer, S. Reipert, G. A. Rezniczek, F. Propst, G. Walko, I. Fischer, J. Bauer, M. W. Leschnik, B. Luscher, J. G. Thalhammer, H. Lassmann, and G. Wiche. 2009. Targeted inactivation of a developmentally regulated neural plectin isoform (plectin 1c) in mice leads to reduced motor nerve conduction velocity. *J. Biol. Chem.* 284:26502-26509.
19. Wiche, G., and L. Winter. 2011. Plectin isoforms as organizers of intermediate filament cytoarchitecture. *Bioarchitecture* 1:14-20.
20. Hansen, J.-P., and I. R. McDonald. 1990. Theory of Simple Liquids. Academic Press, London.
21. Tang-Schomer, M. D., A. R. Patel, P. W. Baas, and D. H. Smith. 2010. Mechanical breaking of microtubules in axons during dynamic stretch injury underlies delayed elasticity, microtubule disassembly, and axon degeneration. *FASEB J.* 24:1401-1410.
22. Yi, J. Y., K. M. Ori-McKenney, R. J. McKenney, M. Vershinin, S. P. Gross, and R. B. Vallee. 2011. High-resolution imaging reveals indirect coordination of opposite motors and a role for LIS1 in high-load axonal transport. *J. Cell Biol.* 195:193-201.
23. Kaasik, A., D. Safiulina, A. Zharkovsky, and V. Veksler. 2007. Regulation of mitochondrial matrix volume. *Am. J. Physiol. - Cell Ph.* 292:C157-163.
24. Schnitzer, M. J., K. Visscher, and S. M. Block. 2000. Force production by single kinesin motors. *Nat. Cell Biol.* 2:718-723.
25. Zar, J. H. 1974. Biostatistical Analysis. Prentice-Hall, Englewood Cliffs, NJ.
26. Yamada, K. M., B. S. Spooner, and N. K. Wessells. 1971. Ultrastructure and function of growth cones and axons of cultured nerve cells. *J. Cell Biol.* 49:614-635.
27. Friede, R. L., and T. Samorajski. 1970. Axon caliber related to neurofilaments and microtubules in sciatic nerve fibers of rats and mice. *Anat. Rec.* 167:379-387.
28. Zwillinger, D. 2003. CRC Standard Mathematical Tables and Formulae. CRC Press, Boca Raton.
29. Perrot, R., and J. P. Julien. 2009. Real-time imaging reveals defects of fast axonal transport induced by disorganization of intermediate filaments. *FASEB J.* 23:3213-3225.
30. Sato, M., T. Z. Wong, D. T. Brown, and R. D. Allen. 1984. Rheological properties of living cytoplasm: a preliminary investigation of squid axoplasm *(Loligo pealei). Cell Motil.* 4:7-23.
31. Hurd, D. D., and W. M. Saxton. 1996. Kinesin mutations cause motor neuron disease phenotypes by disrupting fast axonal transport in *Drosophila*. *Genetics* 144:1075-1085.
32. Gindhart, J. G., Jr., C. J. Desai, S. Beushausen, K. Zinn, and L. S. Goldstein. 1998. Kinesin light chains are essential for axonal transport in *Drosophila*. *J. Cell Biol.* 141:443-454.